Supplementary Information

Defect Passivation in Methylammonium/Bromine Free Inverted Perovskite Solar Cells Using Charge-Modulated Molecular Bonding

Dhruba B. Khadka[1*], Yasuhiro Shirai[1*], Masatoshi Yanagida[1], Hitoshi Ota[2], Andrey Lyalin[3,4*], Tetsuya Taketsugu[4,5], and Kenjiro Miyano[1]

[1] Photovoltaic Materials Group, Center for GREEN Research on Energy and Environmental Materials, National Institute for Materials Science (NIMS), 1-1 Namiki, Tsukuba, Ibaraki 305-0044, Japan

[2]Battery Research Platform, Research Center for Energy and Environmental Materials (GREEN), National Institute for Materials Science (NIMS), Namiki 1-1, Tsukuba 305-0044, Japan

[3]Research Center for Energy and Environmental Materials (GREEN), National Institute for Materials Science, Namiki 1-1, Tsukuba 305-0044, Japan

[4]Institute for Chemical Reaction Design and Discovery (WPI-ICReDD), Hokkaido University, Sapporo 001-0021, Japan

[5]Department of Chemistry, Faculty of Science, Hokkaido University, Sapporo 060-0810, Japan

Corresponding Author

[*]KHADKA.B.Dhruba@nims.go.jp

[*]SHIRAI.Yasuhiro@nims.go.jp

[*]lyalin@icredd.hokudai.ac.jp

Supplemenatry Tables and Supplementary Figures

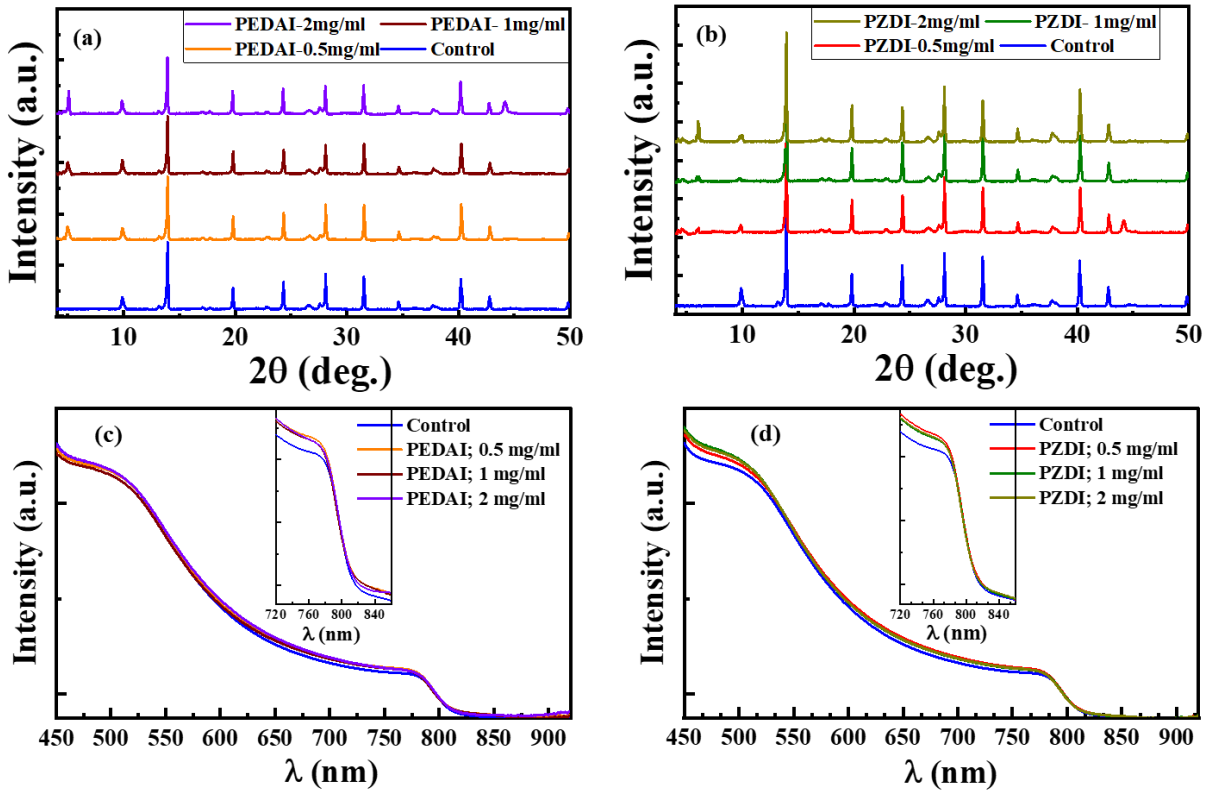

Fig. S1. XRD patterns of MA-free ($FA_{0.84}$ $Rb_{0.04}Cs_{0.12}PbI_3$) films without and with DIM treatments: a) PEDAI or b) PZDI solutions in IPA; 0 (control), 0.5, 1, and 2 mg/ml. c, d) Absorption spectra of respective films.

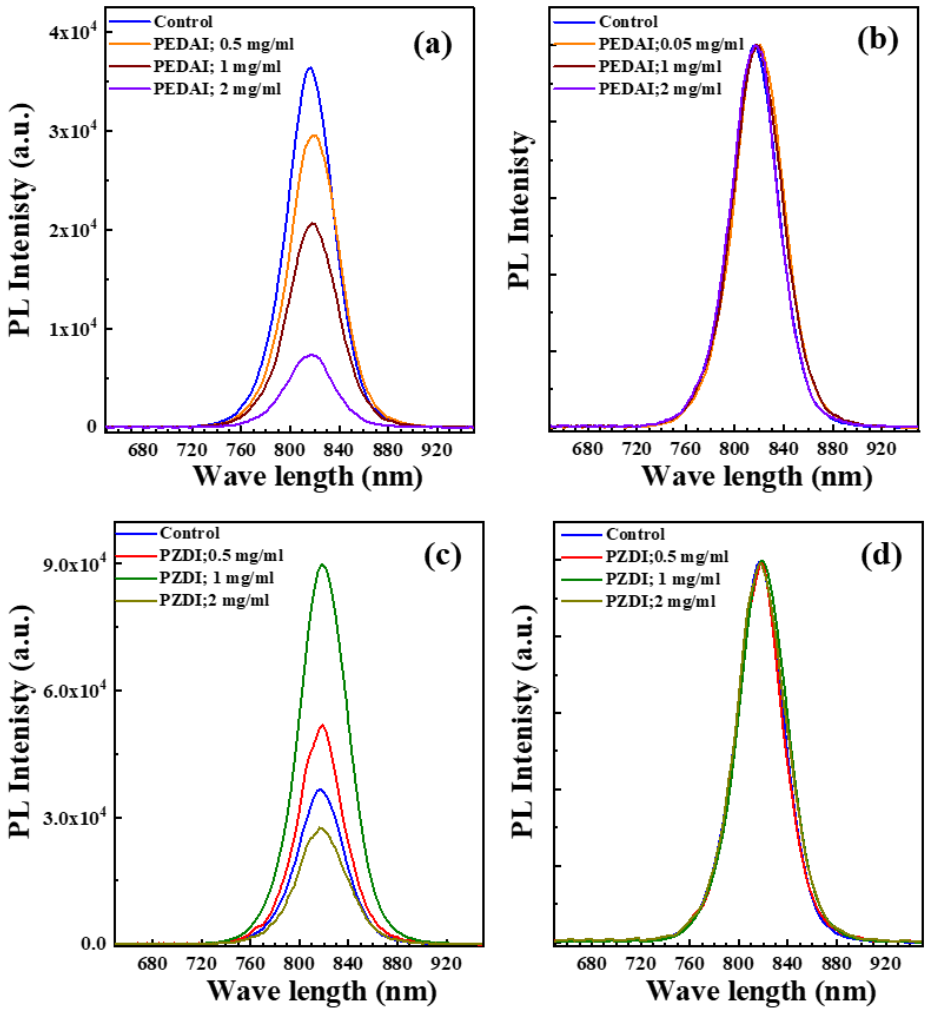

Fig. S2. PL spectra of HP films without and with DIM treatments: a) PEDAI or c) PZDI solutions in IPA; 0 (control), 0.5, 1, and 2 mg/ml. b, d) represent normalized PL spectra of respective films.

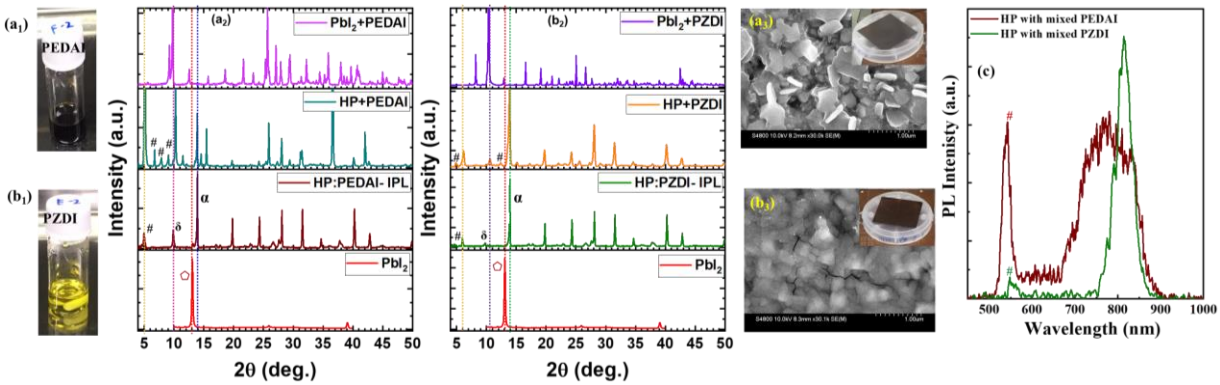

Fig. S3. Photo of mixed HP precursor [a_1) PEDAI or b_1) PZDI and HP/mixed precursor]. a_2, b_2) XRD patterns of PbI_2 film, HP film surface treated with PEDAI or PZDI (dissolved 2 mg/ml in IPA), HP film with mixed PEDAI or PZDI, and powder crystal prepared by mixing PbI_2 and PEDAI or PZDI in 1:2 ratio. Here, # -2D phase with PEDAI or PZDI, ⬠- PbI_2 peak, *δ*- non-photoactive perovskite phase, α-photoactive perovskite phase. a_3, b_3) SEM images of HP film (mixed precursor: PEDAI or PZDI/perovskite-mixed precursor. c) PL spectra of the HP film prepared using mixed precursor. The shoulder response marked with # in PL spectra stems from the 2D phase formed with PEDAI or PZDI. Note that mixed precursor was prepared by mixing 0.5 M-PEDAI or PZDI + 0.5 M PbI_2 and 1M of control precursor ($FA_{0.84}$ $Rb_{0.04}Cs_{0.12}PbI_3$).

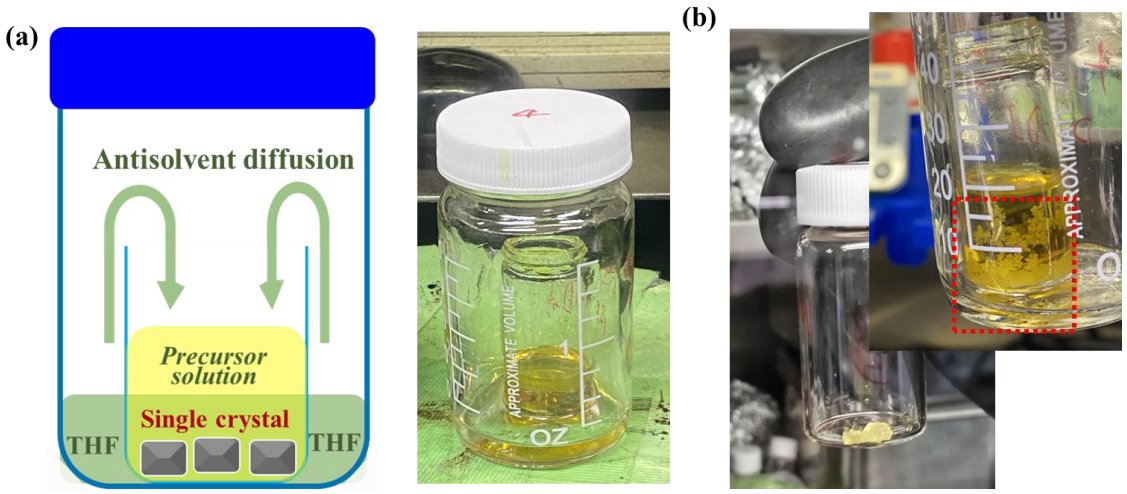

Fig. S4. a) Schematic of synthesis of single crystal by antisolvent vapor-assisted crystallization method. of single crystal sample. b) the vial containing precursor solution was sealed in a bottle and crystal growth (displayed in the rectangle) and crystal separated from the vial.

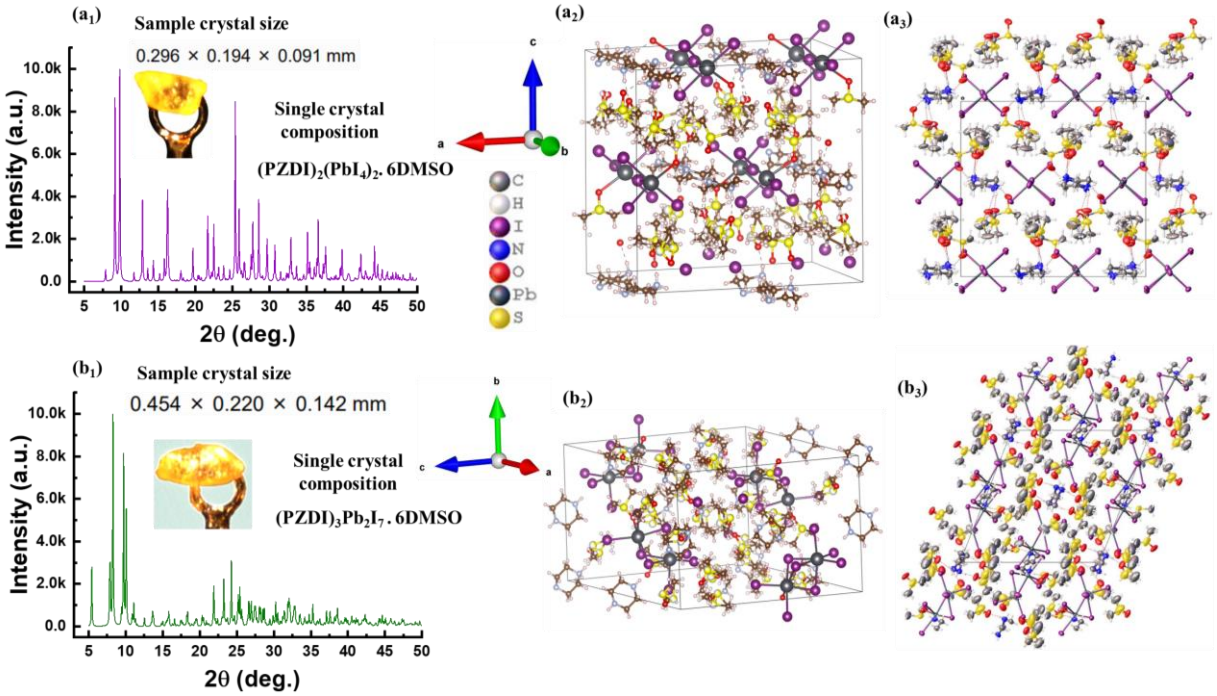

Fig. S5. Analysis of a single crystal obtained by adopting the method as depicted in **Fig. S4**. a_1) simulated PXRD result of crystal (insets are optical image, dimension, and composition: (Single-crystal structure of $PZDI)_2(PbI_4)_2$. 6DMSO (CCDC 2311444)) grown in precursor solution (mixing PZDI and PbI_2 in 2:1 molar ratio), a_2) simulated crystal unit, a_3) Packing diagram. b_1-b_3) corresponding results and properties of the single-crystal structure of $PZDI)_3Pb_2I_7$. 6DMSO (CCDC 2311446) as grown in precursor solution (mixing PZDI and PbI_2 in 1:1 molar ratio).

Table S1. Crystal data and refinement of a corresponding single crystal ($(PZDI)_2(PbI_4)_2$. 6DMSO: CCDC 2311444 and $(PZDI)_3Pb_2I_7$. 6DMSO: CCDC 2311446).

Crystal data	XRD- patterns- Fig. S5a1	XRD- patterns- Fig. S5b1
CIF file	CCDC 2311444	CCDC 2311446
Chemical Formula	$(PZDI)_2(PbI_4)_2$. 6 DMSO	$(PZDI)_3Pb_2I_7$. 6 DMSO
Formula weigh	1037.33	1903.68
Crystal size (mm)	0.354 × 0.192 × 0.089	0.45 × 0.22 × 0.14
$\boldsymbol{\mu}$ (mm^{-1})	11.055	10.968
Radiation type	Mo Kα	Mo Kα
Wavelength (Å)	0.71073	0.71073
Temperature	293(2)	293.00(10)
Crystal system	Orthorhombic	Monoclinic
Space group	Pna21	P 21 /n
a, b, c (Å)	20.3941 (3), 13.7425 (2), 19.2851 (3)	19.4940(3), 14.11900(10), 20.1039(2)
a, b, g (°)	90, 90,90	90, 111.049(2), 90
V ($Å^3$)	5404.96 (14)	5164.09(12)
Z	8	4
	Data collection	
No. of measured	134993	170497
No. of independent	14685	14425
Completeness	1	0.876
R_{int}	0.0498	0.0613
2θmax (°)	61.818	61.998
	Refinement	
R_1 [$F^2 > 2s(F^2)$]	0.0439	0.0395
wR(F2)	0.0978	0.0836
S	1.149	1.167
No. of reflections	14685	14425
No. of parameters	475	435

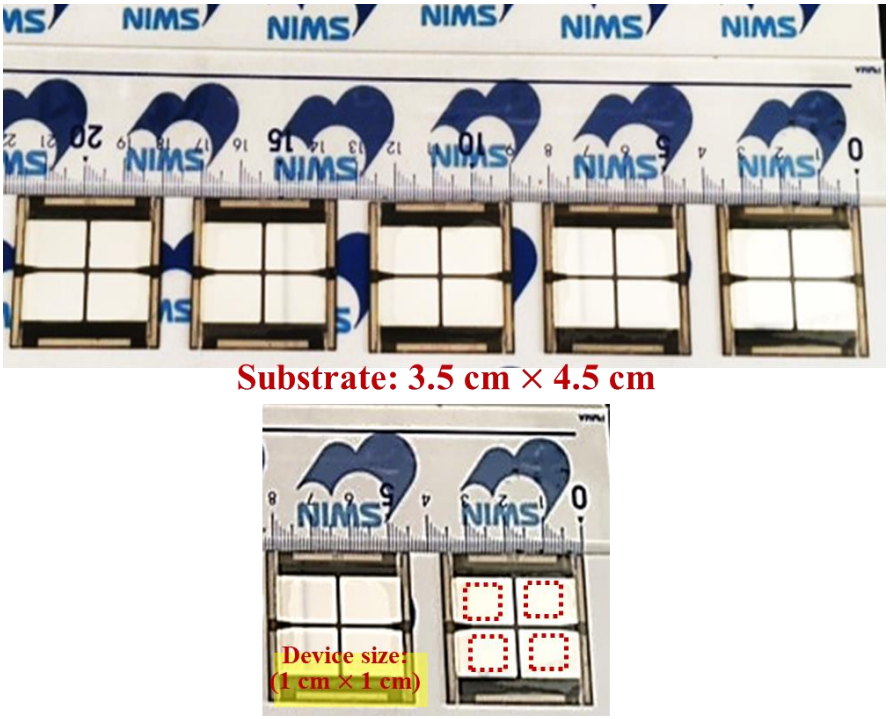

Fig. S6. Photographs of a set of HHPSC devices prepared on ITO substrate (4.5 cm ×3.5 cm) and scale of each device size (1cm×1cm) used for measurement mask.

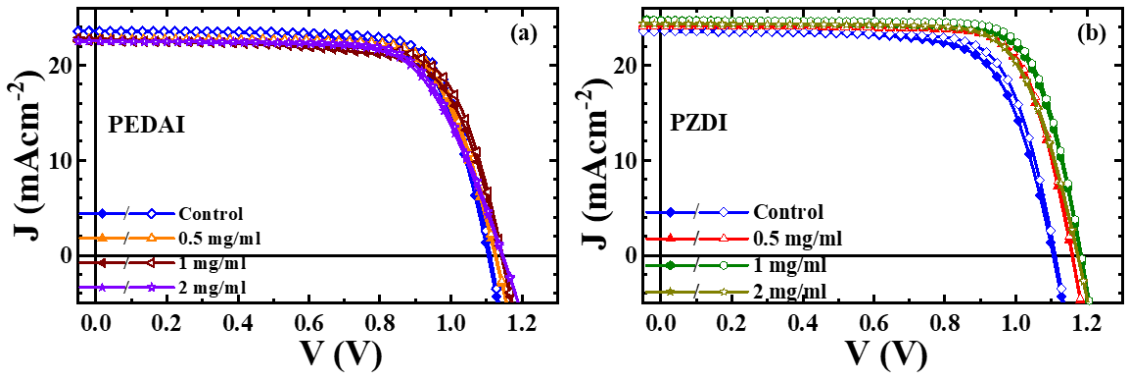

Fig. S7. *J-V* curves of the control and DIM; a) PEDAI or b) PZDI treated HPSCs. ▼/▽ forward /reverse scan direction.

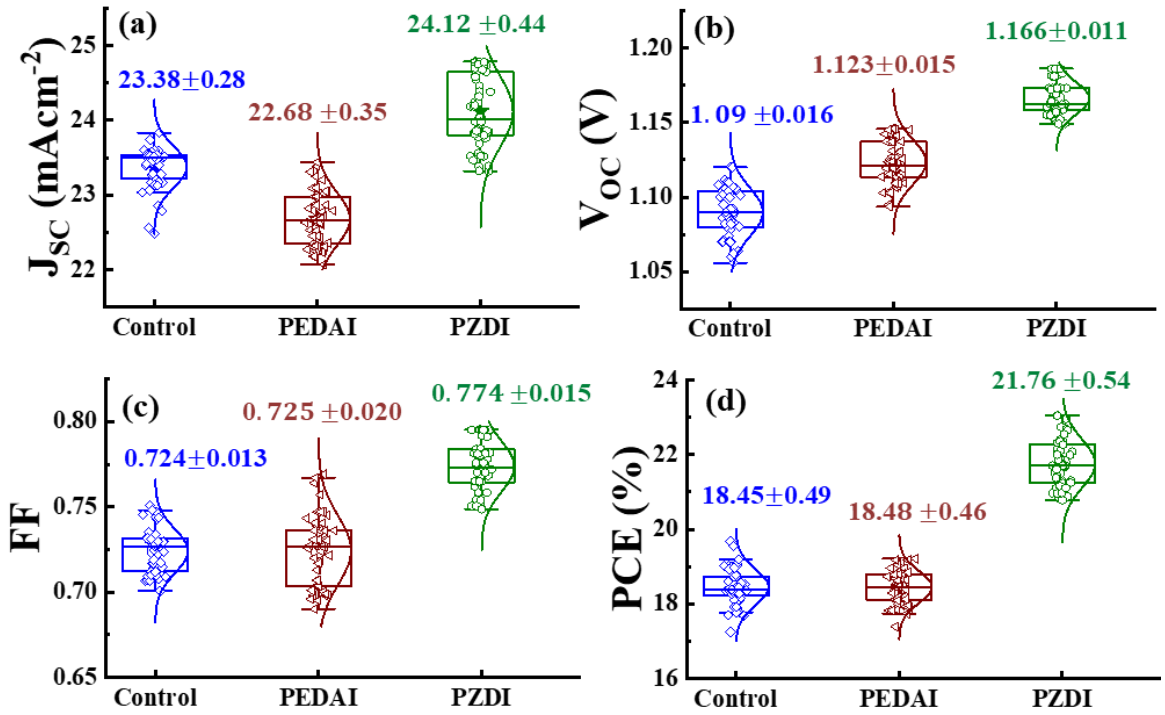

Fig. S8. Statistics of PV characteristic parameters of control and PEDAI or PZDI-treated HPSCs, including; a) V_{OC}, b) J_{SC}, c) *FF*, and d) *PCE*. The data shown above the box distribution corresponds average and standard deviation for corresponding device parameters. These data consist of 50 devices from 6 batches.

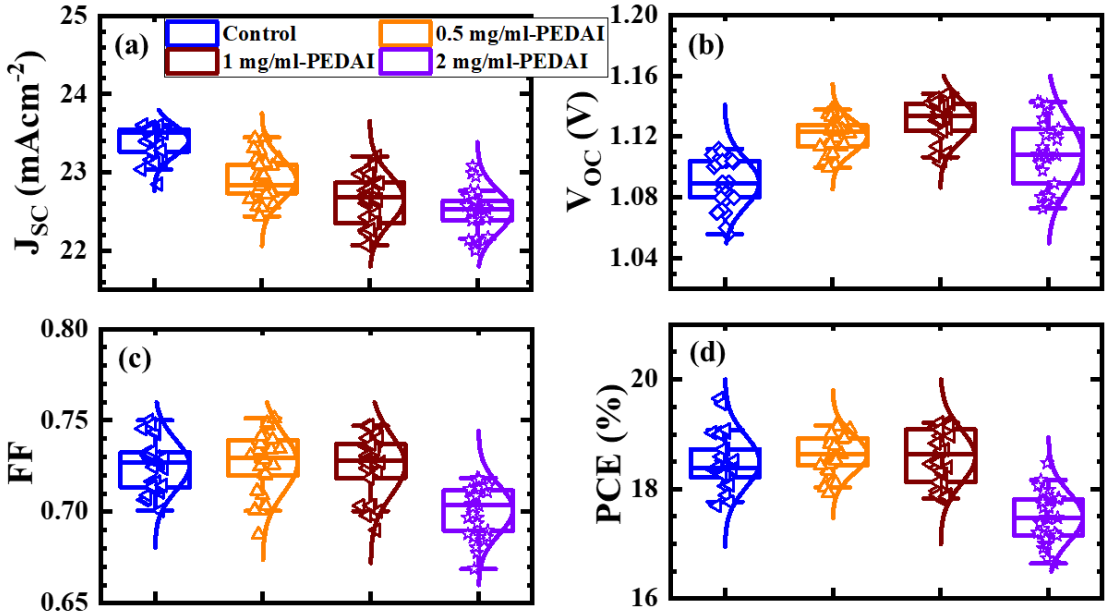

Fig. S9. Statistics of PV characteristic parameters of control and PEDAI-treated HPSCs, including; a) V_{OC}, b) J_{SC}, c) *FF*, and d) *PCE*. These data consist of 30 devices from 4 batches.

Table S2. Photovoltaic parameters of the best-performing HPSCs with MA-free HP (without and with PEDAI surface treatment). The parameters given inside the parentheses represent the average values and standard deviation.

Device/parameters	Control	0.5 mg/ml	1 mg/ml	2 mg/ml
J_{SC} (mAcm^{-2})	23.56 (23.41 ±0.21)	22.75 (22.91±0.26)	22.73 (22.66±0.31)	22.67 (23.51±0.27)
V_{OC} (V)	1.112 (1.089 ±0.016)	1.132 (1.118 ±0.014)	1.145 (1.131 ±0.013)	1.142 (1.114 ±0.022)
FF	0.750 (0.725 ±0.014)	0.745 (0.726 ±0.016)	0.738 (0.725 ±0.016)	0.702 (0.701 ±0.013)
PCE (%)	19.64 (18.51 ±0.48)	19.18 (18.61 ±0.394)	19.22 (18.89 ±0.48)	18.17 (17.49 ±0.46)

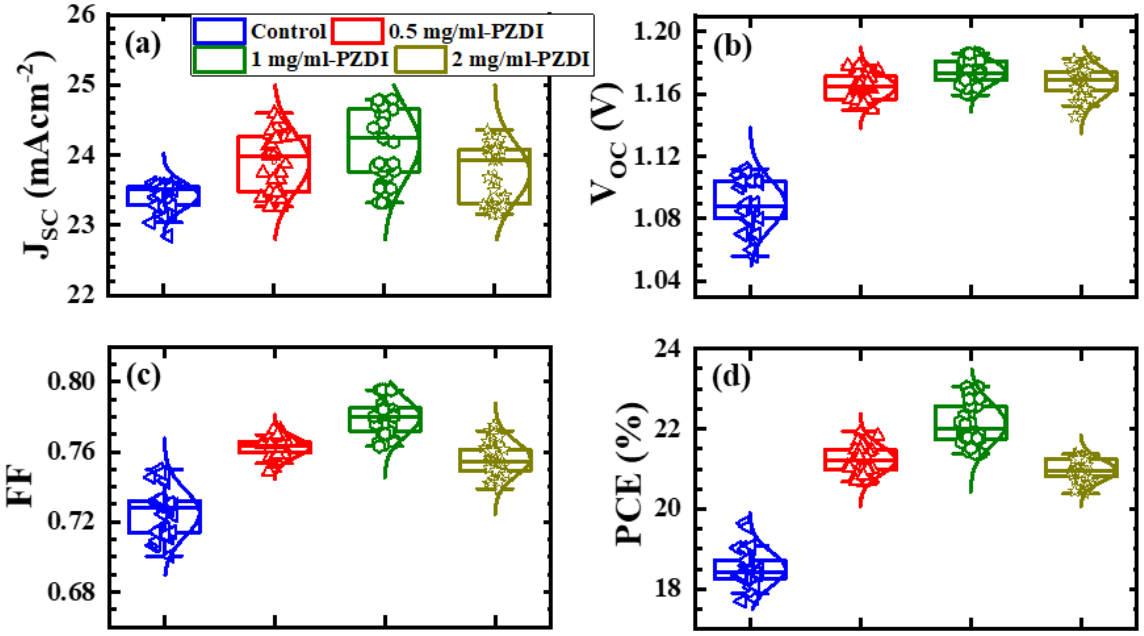

Fig. S10. Statistics of PV characteristic parameters of control and PZDI treated HPSCs, including; a) V_{OC}, b) J_{SC}, c) *FF*, and d) *PCE*. These data consist of 30 devices from 4 batches.

Table S3. Photovoltaic parameters of the best-performing HPSCs with MA-free HP (without and with PZDI surface treatment). The parameters given inside the parentheses represent the average values and standard deviation.

Device/parameters	Control	0.5 mg/ml	1 mg/ml	2 mg/ml
J_{SC} (mAcm^{-2})	23.56 (23.41 ±0.21)	24.63 (23.97 ±0.42)	24.79 (24.15 ±0.51)	24.54 (23.71 ±0.43)
V_{OC} (V)	1.112 (1.089 ±0.016)	1.181 (1.663 ±0.009)	1.186 (1.176 ±0.008)	1.174 (1.168 ±0.011)
FF	0.750 (0.725 ±0.014)	0.765 (0.762 ±0.006)	0.784 (0.775 ±0.012)	0.756 (0.752 ±0.013)
PCE (%)	19.64 (18.51 ±0.48)	22.25 (21.27 ±0.39)	23.05 (22.35 ±0.54)	21.78 (20.95 ±0.49)

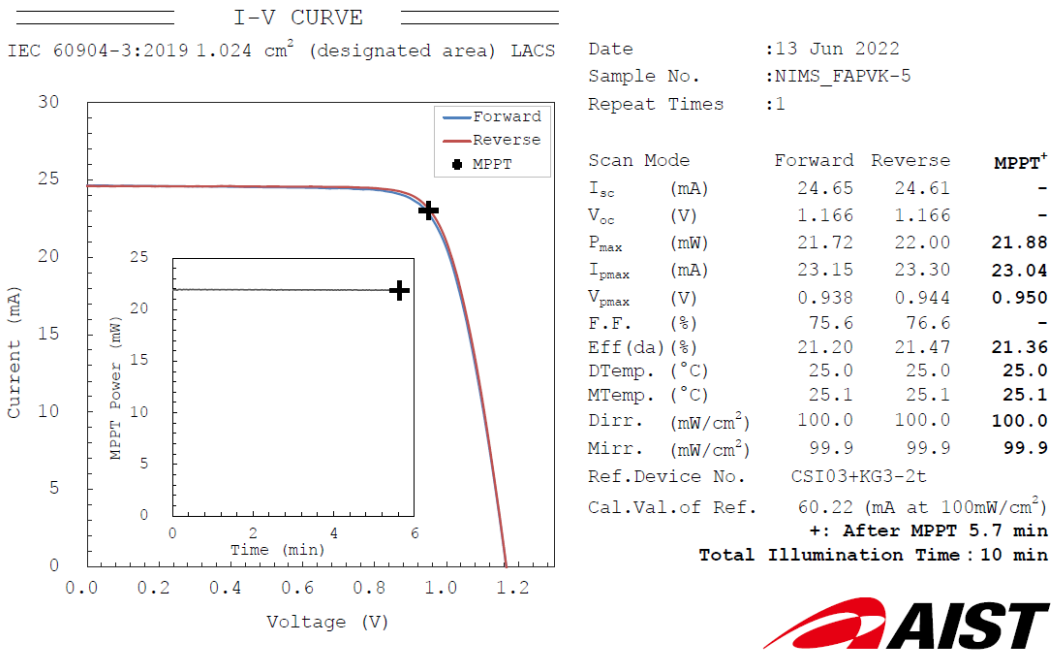

Fig. S11. Certified results from an accredited photovoltaic certification laboratory (AIST, Japan). The certified PCE is 21.36% - certified aperture with an area of ~1.024 cm^2. The certified J-V curves with double scanning give PCE forward: 21.20% and PCE reverse: 21.47%. (HP film: $Rb_{0.4}Cs_{0.12}FA_{0.84}PbI_3$ with PZDI surface treatment).

Table S4. Summary of certified/record device large area (1 cm^2) reports (Pb-HP using multiple cations, anions, functional additives, and interfacial layer).

Device Type	Device Structure	Perovskite	Additive	Area (cm^2)	PCE (%)	Reported Efficiency	date	Ref.
Regular (n-i-p)	ITO/c-TiO_2/TiO_2 nanorods/PMMA:PCBM/ **Perovskite**/PMMA/Spiro-OMeTAD)/MoOx/IZO/**Au**	(Cs,FA,MA)Pb(I,Br)$_3$	-----	1.0	21.6	Certified	2021	1
Regular (n-i-p)	FTO/TiO_xN_y/meso-TiO_2/PMMA: PCBM/ **perovskite**/PMMA/P_3HT: CuPc/**Au**	(Cs,FA,MA)Pb(I,Br)$_3$	0.01 M-$PbCl_2$/MACl	1.0	22.6	Certified	2022	2
Regular (n-i-p)	FTO/SnO2/ **perovskite**/spiro-OMeTAD/EVA/**Cu-Ni-Graphene**	FAMAPb(I,B_r)3	-----	0.09	24.37	Certified	2022	3
				1.02	20.76			
Inverted (p-i-n)	ITO/NiOx-nanoparticles/ (IL)EMDP/ **Perovskite**/PCBM/BCP/**Au**	(Cs,FA,MA)Pb(I,B_r)$_3$	-----	1.01	20.91	Not certified	2021	4
Inverted (p-i-n)	ITO/PTAA/PIC-Al_2O_3/ **Perovskite**/C60/BCP/**Ag**	(FA,MA)CsPb(I,Br)$_3$	MACl	0.06	24.9	certified	2023	5
				1.06	23.30			
Regular (n-i-p)	ITO/SnO_2/perovskite/Spiro-OMeTAD/Au	(Cs,FA)PbI_3	4-MeO-PEAI	1.00	23.7	certified	2022	6
Regular (n-i-p)	FTO/SnO_2/perovskite/ Spiro-OMeTAD/ Au	(Cs,FA,MA)Pb(I,Br,Cl)$_3$	2-Cl-PEAI	0.1	23.9	certified	2023	7
				1.00	23.7			
Regular (n-i-p)	FTO/SnO_2(ALD)/PCBM/PMMA/**Perovskite**/PMMA/Spiro/**Au**	(Rb,Cs,FA)PbI_3	-----	0.1024	20.35	Not certified	2018	8
Regular (n-i-p)	FTO/TiO_2/perovskite/ Spiro-OMeTAD/ Au	(Cs,FA)PbI_3	CoFAc	0.09	24.64	Not certified	2023	9
Inverted (p-i-n)	ITO/2PACz/**Perovskite/PEACl**/C_{60}/BCP/**Au**	(Cs,FA)PbI_3	PEACl	0.123	22.3	Not Certified	2021	10
Inverted (p-i-n)	ITO/NiOx-iink/**Perovskite**/C_{60}/BCP/**Cu**	(Cs,FA,)Pb(I,SCN)$_3$	TCMAI-doping	0.04	23.2	Certified	2023	11
Inverted (p-i-n)	ITO/NiOx-sputtered/MeO/**Perovskite**/ PZDI/C_{60}/BCP/**Ag**	(Rb,Cs,FA)PbI_3	PZDI	1.024	21.47 (23.17)	Certified	*This work (Record certify PCE for inverted device structure)	

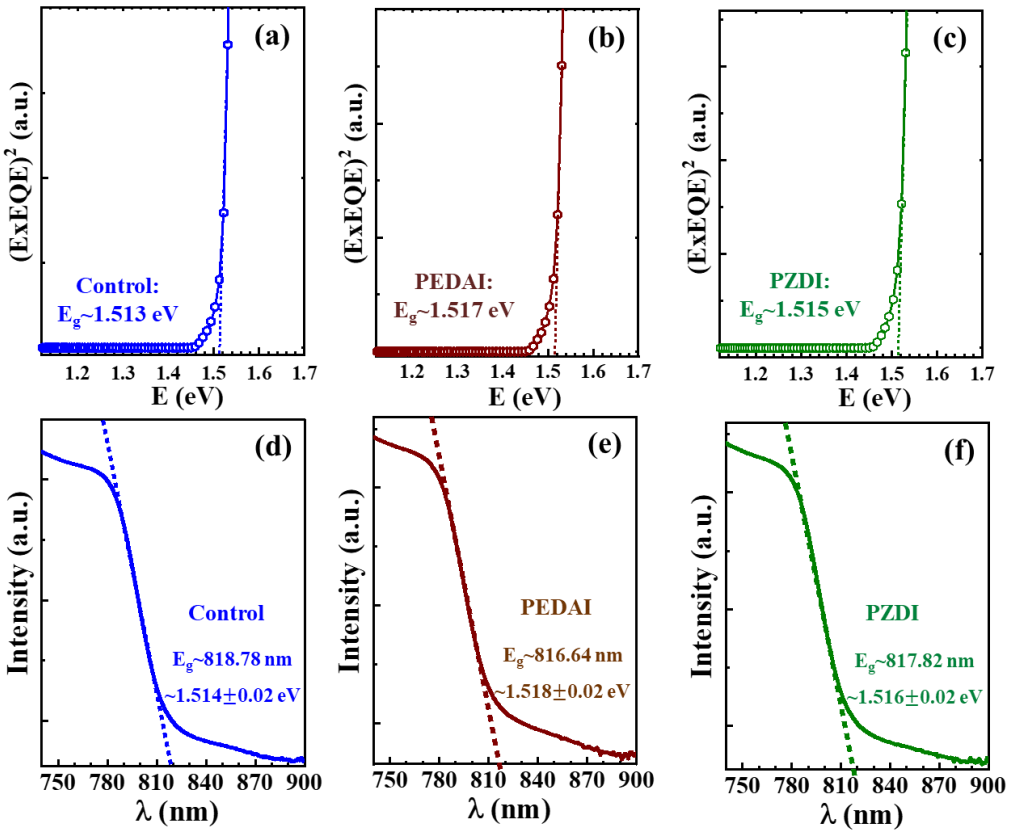

Fig. S12. Estimation of bandgap energy (E_g) of HP layers (control and with surface treatment (PEDAI or PZDI)). a-c) E_g estimated from *EQE* analysis. d-f) E_g calculated from absorption spectra of respective films.

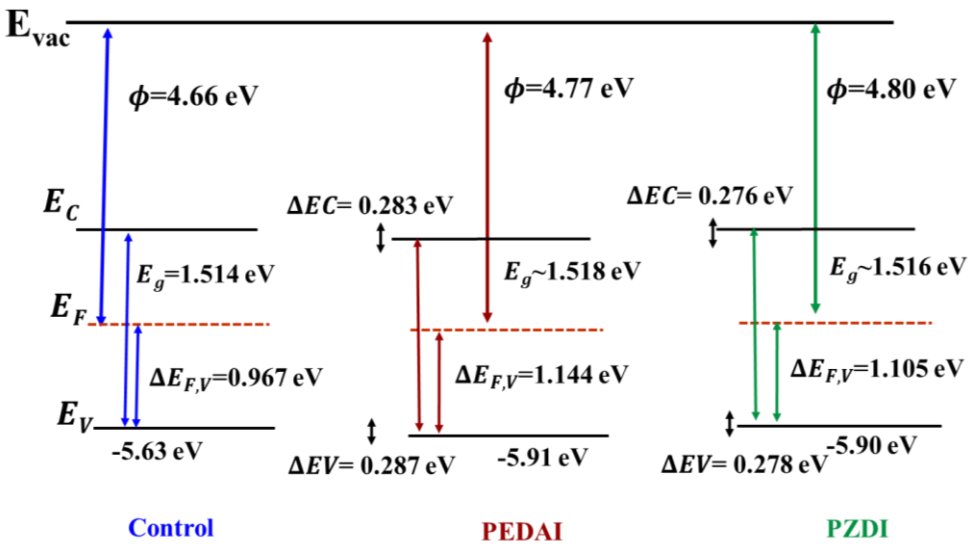

Fig. S13. Energy band schematics of control and PEDAI or PZDI treated film extracted from UPS spectra. Note that E_g for this schematic is calculated from absorption spectra (s Fig. S12d-f).

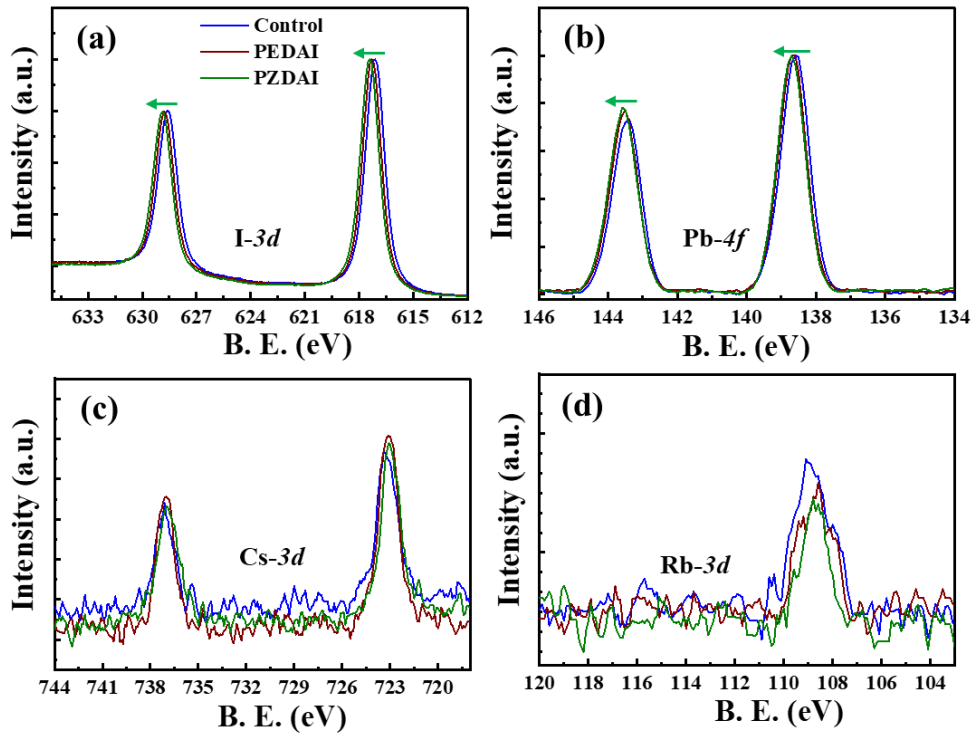

Fig. S14. XPS-spectra for the control and PEDAI or PZDI treated films; a) I-*3d* core, b) Pb-*4f*, c) Cs-*3d* core, and d) Rb-*3d* core. The arrowhead indicates the shifting direction of the XPS Characteristic peak.

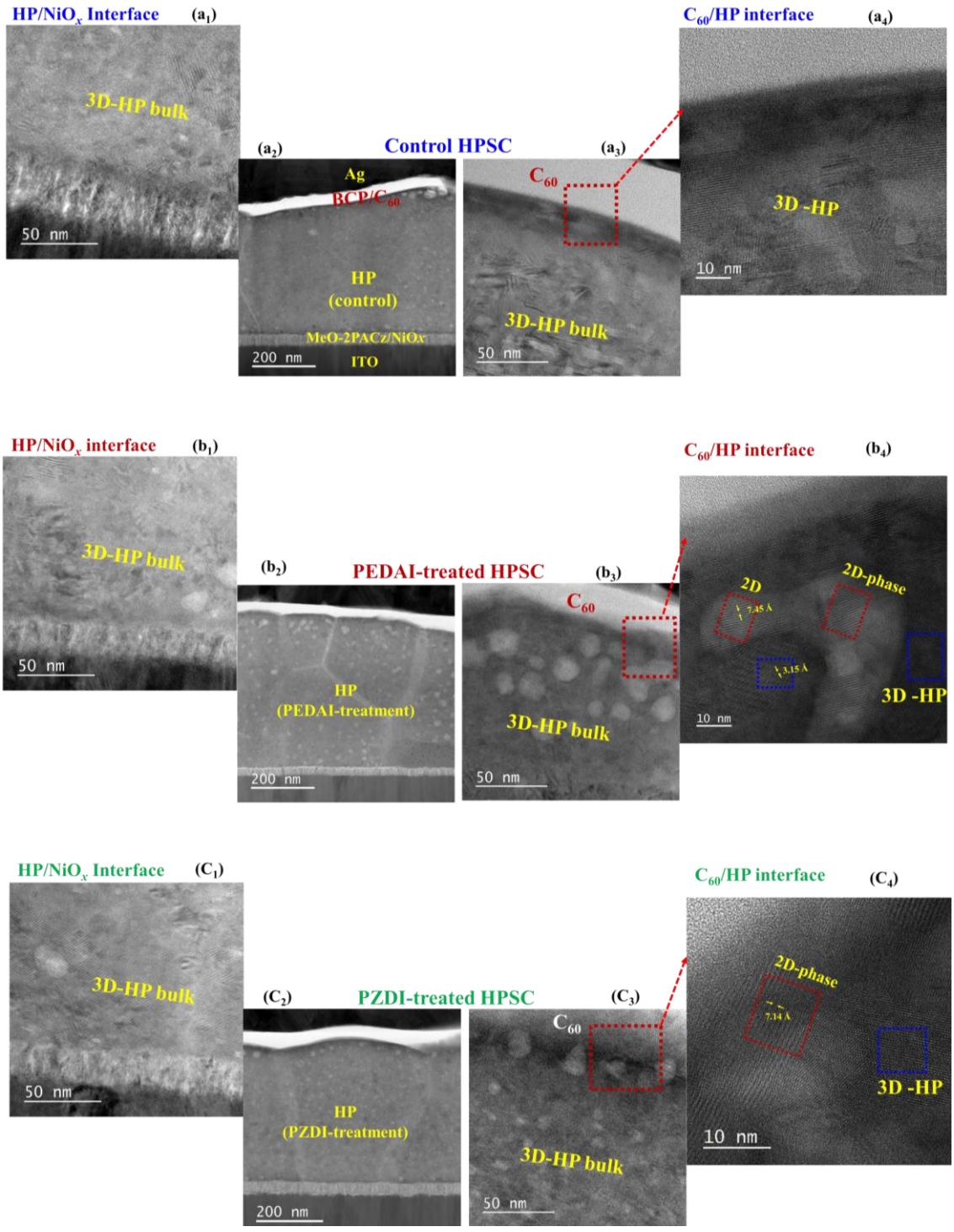

Fig. S15. Cross-sectional HR-TEM image of HPSCs for interface analysis; control (a_1-a_4), PEDAI-treated (b_1-b_4), and PZDI-treated (c_1-c_4). HP/NiO_x interface (a_1,b_1,c_1)), over all cross-section (a_2,b_2,c_2), C_{60}/HP interface ((a_3,b_3,c_3), and interface of C_{60}/HP top surface (a_4,b_4,c_4). Note that the surface passivation with PEDAI forms a rich 2D phase at the interface and grain boundaries. On the other hand, PZDI surface treatment grows with an evenly distributed 2D phase interface on the surface of 3D-HP with diffusion through grain boundaries to some extent.

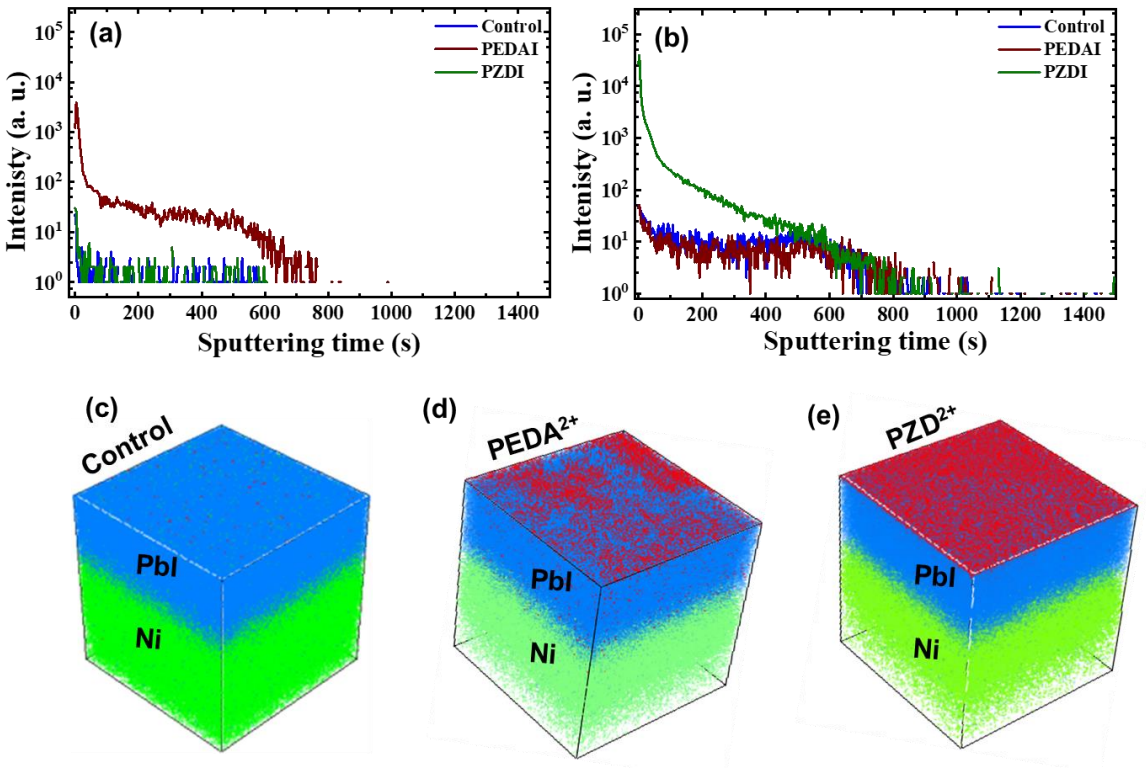

Fig. S16. ToF-SIMS depth profiles of control and surface-treated HP film. a) $PEDA^{2+}$ distribution and b) PZD^{2+} distribution in control and DIM-treated HP films. Reconstructed 3D maps; Distributions of passivated molecules in HP film c) control, d) PEDAI-treated, and e) PZDI-treated.

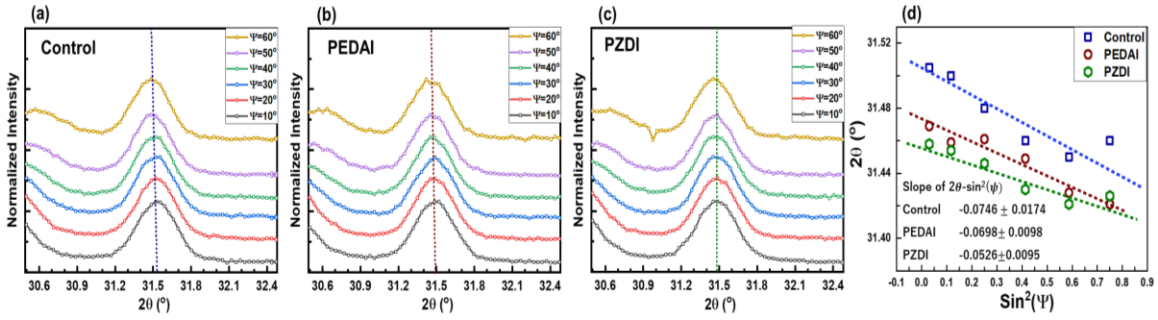

Fig. S17. XRD spectrum at different tilt angles for a) control, b) PEDAI, and c) PZDI devices, respectively. d) Residual strain extracted from the corresponding HPSC device' diffraction strain data as a function of $\sin^2\psi$.

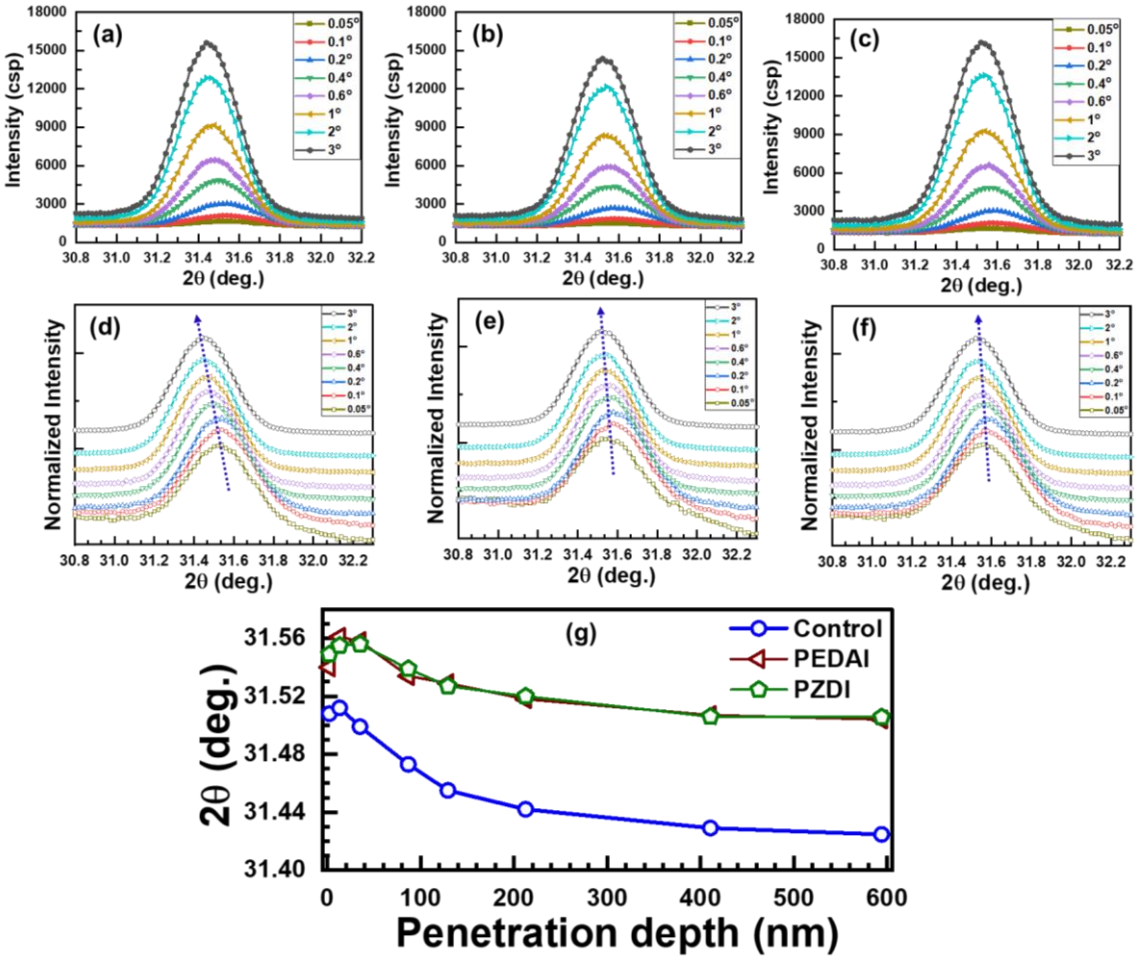

Fig. S18. GIXRD spectra: a, d) control, b, e) PEDAI, and c, f) PZDI. g) plot of penetration depth corresponds to the grazing incident angle. X-ray attenuation length (penetration depth) into the perovskite film (estimated density ~3.86 gcm^{-3}) was calculated using a report by Davis and co-workers (Atomic Data and Nuclear Data Tables, 1993, 54, 181-342) and Rigaku-manual.

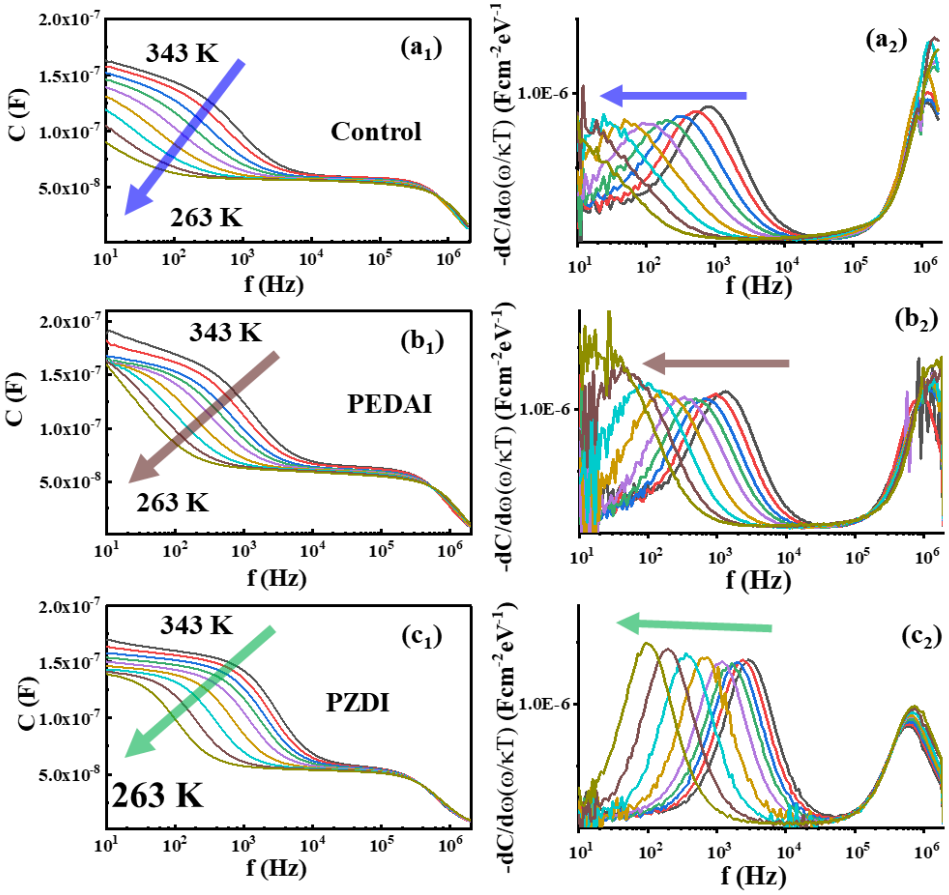

Fig. S19. Thermal admittance spectra (*TAS*). a_1-c_1) *C-f-T* spectra of control and PEDAI or PZDI treated devices. a_2-c_2) differentiation of respective *C-f-T* spectra for determination of inflection frequencies.

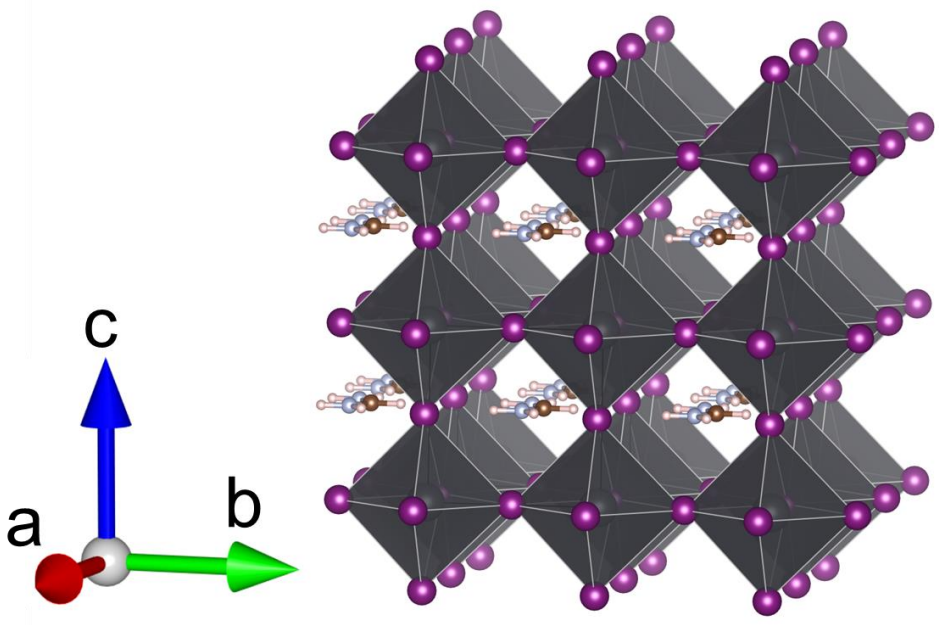

Fig. S20. The optimized pseudo-cubic structure of the bulk $FAPbI_3$. Pb atoms are colored grey, I atoms are purple, C atoms are brown, N atoms are light grey, and H atoms are light pink. The orientation of the lattice axes (a/b/c and arrows) is shown in the insert. Figure was created using VESTA software.[12]

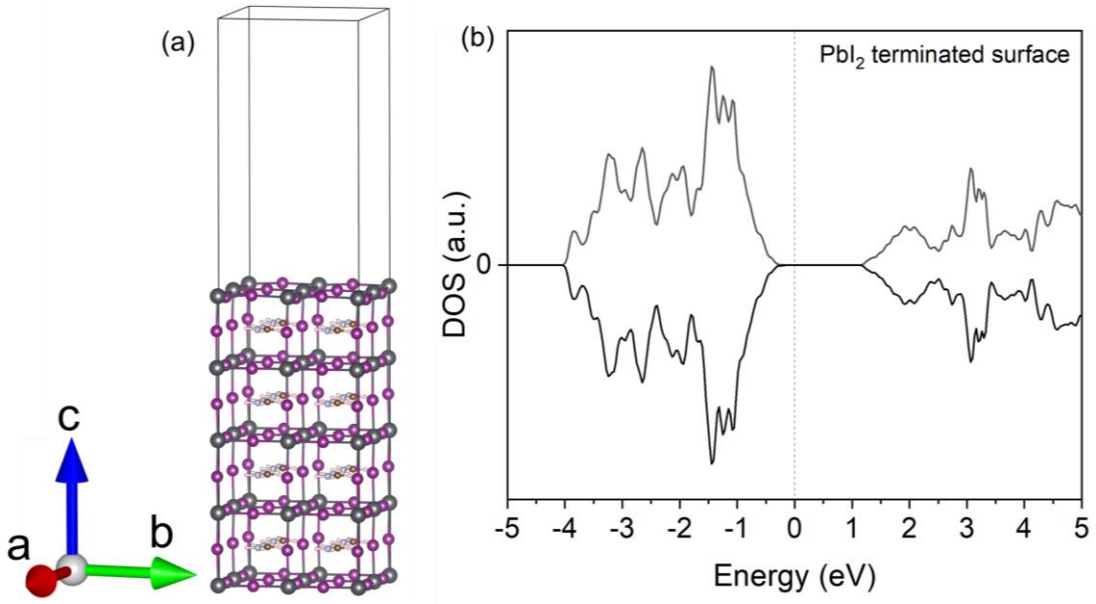

Fig. S21. a) The optimized structure of the 2x2 unit cell of PbI_2-terminated surface (001) of the pseudo-cubic $FAPbI_3$. b) Total density of states calculated for the defect-free PbI_2-terminated surface of $FAPbI_3$. The orientation of the lattice axes (a/b/c and arrows) is shown in the insert. Figure in (a) was created using VESTA software.[12]

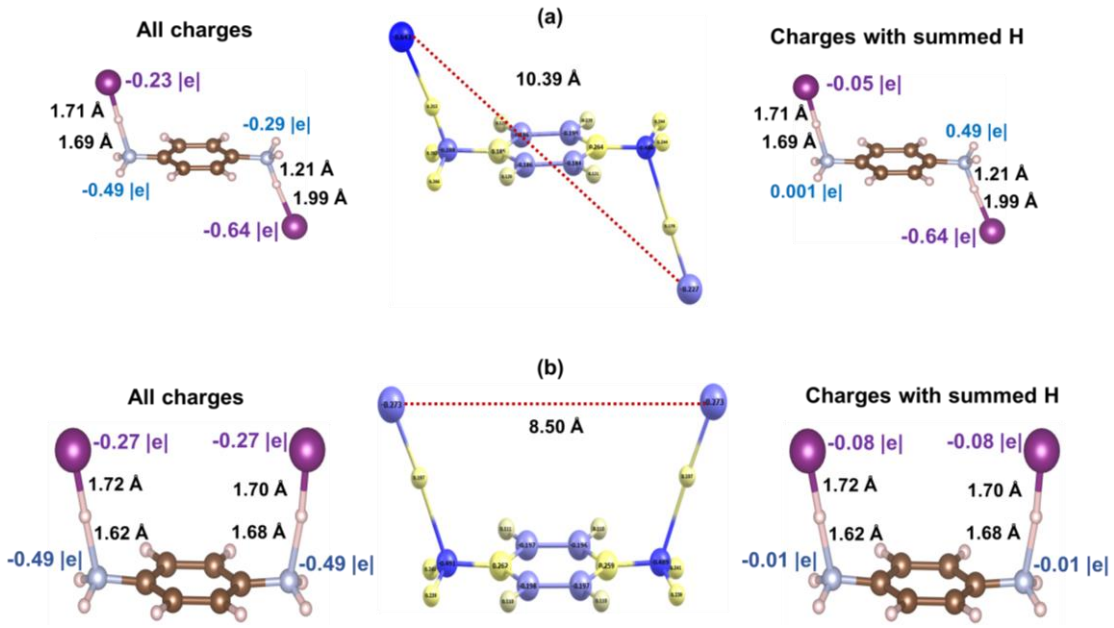

Fig. S22. The optimized structures of a free 1,4-phenylenediamine dihydriodide (PEDAI), $C_6H_8N_2$*2HI, molecule. (a) The most stable *trans*-isomer structure, and (b) the low-energy *cis*-isomer form. Mulliken charges or Mulliken charges with summed H (iodine and nitrogen atoms) were calculated at the B3LYP/def2TZVP level of theory with the use of Gaussian 09.[17]

Free 1,4-phenylenediamine dihydriodide (PEDAI), $C_6H_8N_2$*2HI, molecules possess several isomeric forms depending on the position of the HI compounds. The most stable *trans*-isomer is shown in Figure S18a, while its *cis* form (Fig. S22b) is only 0.086 eV less stable. When PEDAI adsorbs on the PbI_2-terminated surface of $FAPbI_3$ adsorption of the *cis*-form became energetically favorable, as it maximizes interaction of I atoms of PEDAI with the surface Pb atoms.

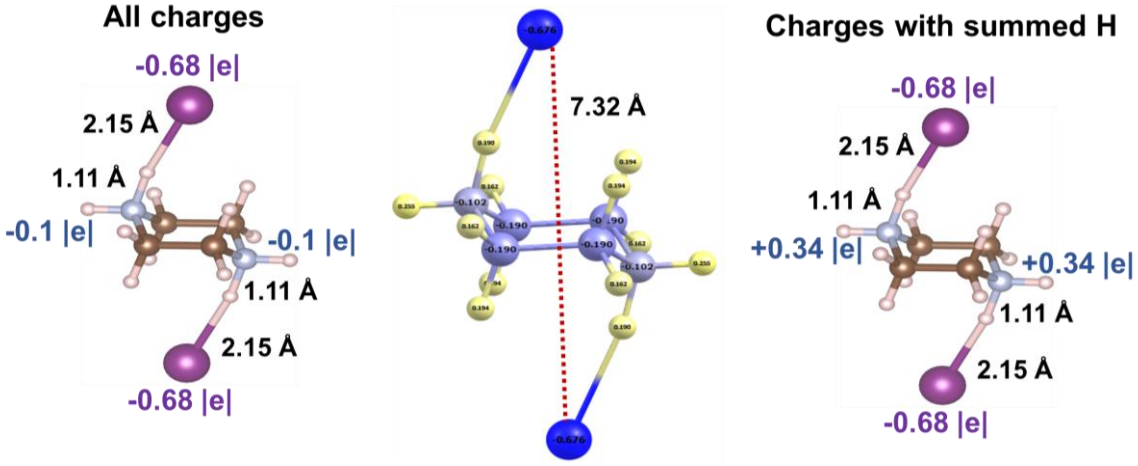

Fig. S23. The optimized structure of a free piperazine dihydriodide (PZDI), $C_4H_{10}N_2$*2HI, molecule. Mulliken charges were calculated at the B3LYP/def2TZVP level of theory with the use of Gaussian 09.[18]

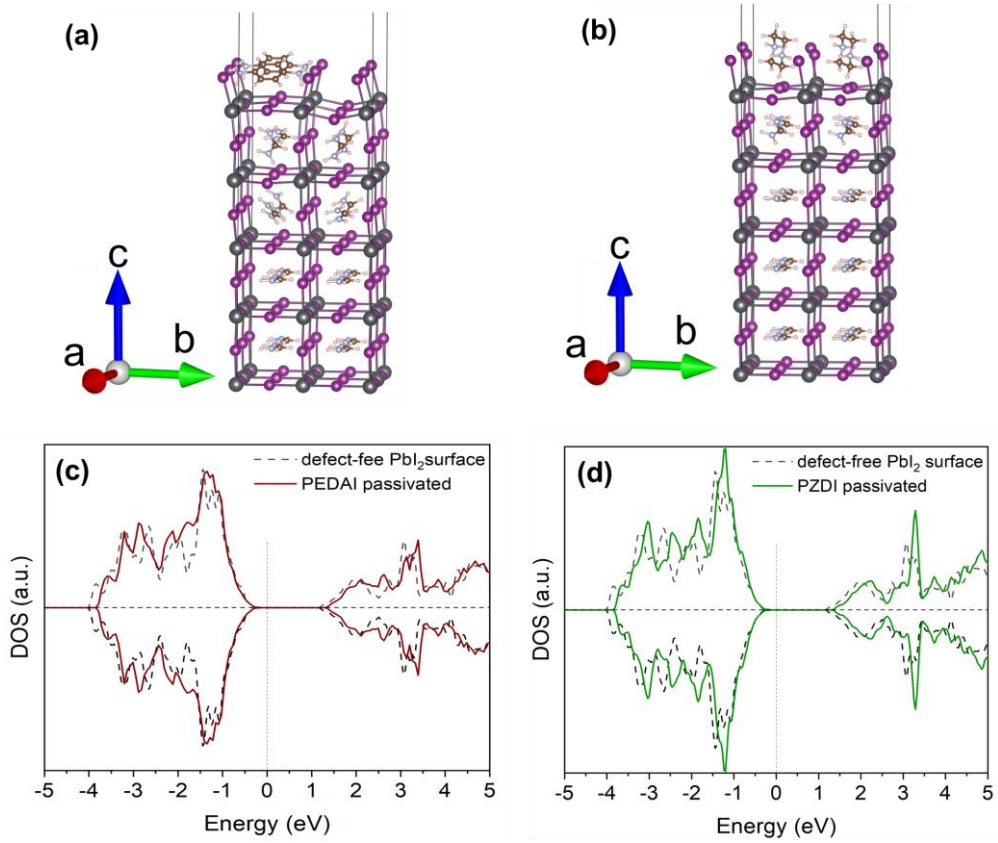

Fig. S24. Optimized structures of a) PEDAI and b) PZDI adsorbed on the defect-free PbI_2-terminated surface of $FAPbI_3$. The spin-polarized total DOS calculated for the PbI_2-terminated surface of $FAPbI_3$ covered by c) PEDAI and d) PZDI. The orientation of the lattice axes (a/b/c and arrows) is shown in the insert. Figures in a) and b) were created using VESTA software.[12]

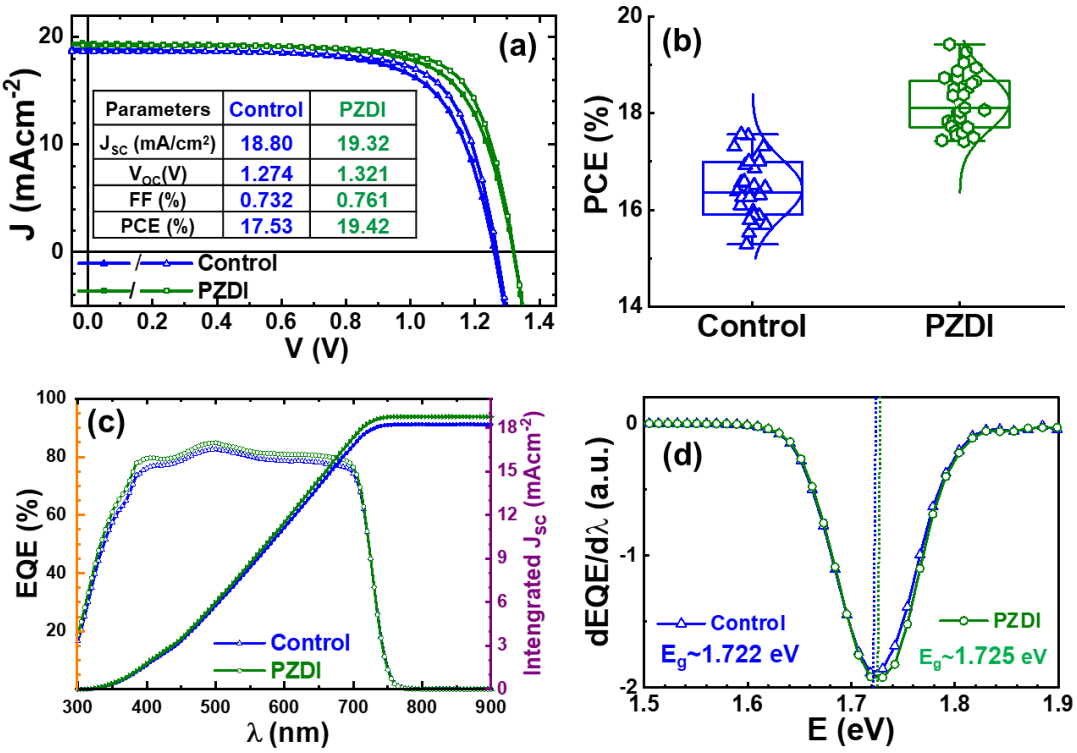

Fig. S25. Device characteristics for wide bandgap-HP (Pb-HP; $FA_{0.84}Cs_{0.12}Rb_{0.04}Pb(I_{0.63}Br_{0.37})_3$) *(WB-HP)*. a) *J-V* curves (device parameters, Table S5) (filled/open symbol- forward /reverse scan direction) of control and PZDI-treated HPSCs. b) PCE statistics of devices. c) *EQE* spectra of respective devices. The values of integrated J_{SC} extracted from *EQE* spectra; 18.22 and 18.78 mAcm^{-2}. (d) Estimation of bandgap energy (E_g) from EQE analysis.

Table S5. Photovoltaic parameters of the best-performing WB-HPSCs corresponding to J-V curves (**Fig. S25**). F and R- scan stand for forward and reverse scan directions. The statistical data (control or PZDI treatment) are taken from 30 devices (average (avg) and standard deviation (sd)) from 5 batches.

Device parameters	*WB-HPSCs*					
	Control			PZDI		
	F-scan	R-scan	statistics (avg±sd)	F-scan	R-scan	Statistics (avg±sd)
J_{SC} (mA/cm^2)	18.86	18.80	18.68 ±0.62	19.43	19.32	19.08 ±0.114
V_{OC} (V)	1.262	1.274	1.26 ±0.003	1.316	1.321	1.312 ±0.002
FF	0.695	0.732	0.709 ±0.004	0.724	0.761	0.724 ±0.017
PCE (%)	16.54	17.53	16.76 ±0.69	18.51	19.42	18.46 ±0.42

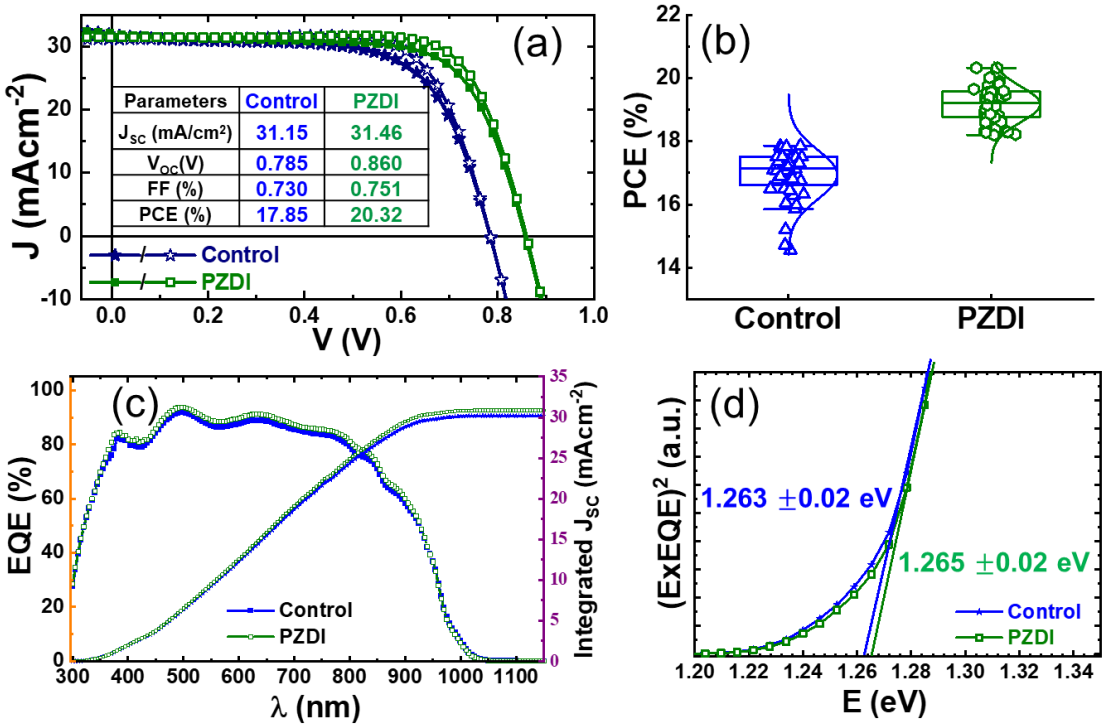

Fig. S26. Device characteristics for narrow bandgap-HP (Sn-Pb-HP; $FA_{0.85}MA_{0.1}Cs_{0.05}(Pb_{0.5}Sn_{0.5})I_3$) *(NB-HP)*. a) *J-V* curves (device parameters, Table S6) (filled/open symbol- forward /reverse scan direction) of control and PZDI-treated HPSCs. b) PCE statistics of devices. c) *EQE* spectra of respective devices. The values of integrated J_{SC} extracted from *EQE* spectra; 30.19 and 30.86 mAcm^{-2}. d) Estimation of bandgap energy (E_g) from EQE analysis.

Table S6. Photovoltaic parameters of the best-performing NB-HPSCs corresponding to J-V curves (**Fig. S26**). F and R- scan stand for forward and reverse scan directions. The statistical data (control or PZDI treatment) are taken from 30 devices (average (avg) and standard deviation (sd)) from 5 batches.

Device parameters	*NB-HPSCs*					
	Control			PZDI		
	F-scan	R-scan	statistics (avg±sd)	F-scan	R-scan	Statistics (avg±sd)
J_{SC} (mA/cm^2)	31.87	31.15	29.78 ±1.05	31.99	31.46	31.74 ±0.64
V_{OC} (V)	0.784	0.785	0.80 ±0.033	0.858	0.860	0.840 ±0.008
FF	0.669	0.730	0.707 ±0.028	0.697	0.751	0.720 ±0.023
PCE (%)	16.74	17.85	16.96 ±0.77	19.14	20.32	19.17 ±0.56

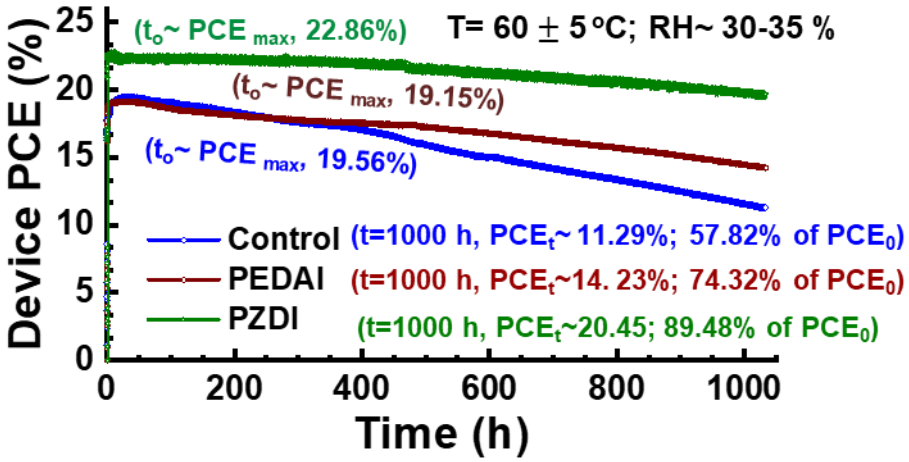

Fig. S27. Stability of the control, PEDAI, and PZDI passivated HPSCs. Non-normalized stability data operational tracking under MPPT conditions: T=60 ±5 °C; RH~ 30–35% (ISOS-L-2) (corresponding to Fig. 6a)

Table S7. Photovoltaic parameters of corresponding aged devices.

Parameters/ Time (h)	control device				PEDAI treated				PZDI treated			
	J_{SC} (mAcm^{-2})	V_{OC} (V)	*FF*	*PCE*	J_{SC} (mAcm^{-2})	V_{OC} (V)	*FF*	*PCE*	J_{SC} (mAcm^{-2})	V_{OC} (V)	*FF*	*PCE* (%)
0	23.36	1.113	0.751	19.53	22.94	1.142	0.731	19.15	24.54	1.188	0.784	22.86
100	23.56	1.113	0.750	19.67	22.75	1.143	0.716	18.62	24.3	1.188	0.777	22.43
500	20.73	1.113	0.690	15.92	21.9	1.142	0.69	17.26	23.27	1.191	0.767	21.26
1000	15.36	1.114	0.660	11.29	18.55	1.145	0.67	14.23	22.66	1.194	0.756	20.45

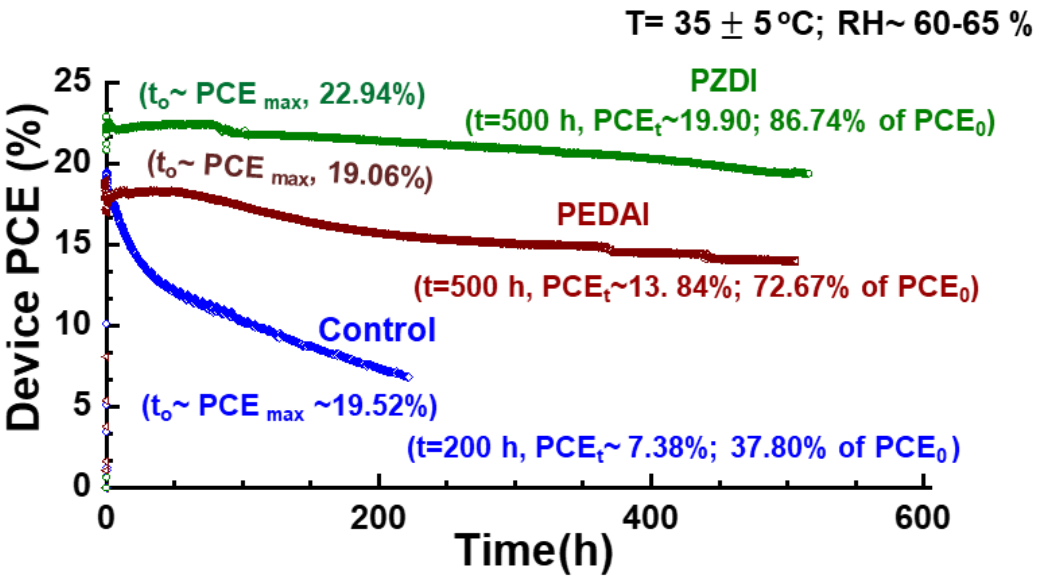

Fig. S28. Stability of the control, PEDAI, and PZDI passivated HPSCs. Non-normalized stability data operational tracking under MPPT conditions: T=35 ±5 °C; RH~ 60–65% (ISOS-L-3) (corresponding to **Fig. 6b**).

Table S8. Photovoltaic parameters of corresponding aged devices.

Parameters/ Time (h)	Control device				PEDAI treated				PZDI treated			
	J_{SC} (mAcm^{-2})	V_{OC} (V)	*FF*	*PCE*	J_{SC} (mAcm^{-2})	V_{OC} (V)	*FF*	*PCE*	J_{SC} (mAcm^{-2})	V_{OC} (V)	*FF*	*PCE (%)*
0	23.62	1.104	0.717	19.52	22.98	1.146	0.724	19.07	24.5	1.188	0.788	22.94
100	19.16	1.03	0.52	10.23	21.28	1.145	0.712	17.35	23.74	1.188	0.775	21.86
200	16.16	1.016	0.45	7.38	19.94	1.143	0.69	15.73	23.35	1.189	0.772	21.43
500					17.76	1.144	0.68	13.82	21.81	1.191	0.766	19.90

References

1. Peng, J. *et al.* Nanoscale localized contacts for high fill factors in polymer-passivated perovskite solar cells. *Science* **371**, 390–395 (2021).

2. Peng, J. *et al.* Centimetre-scale perovskite solar cells with fill factors of more than 86 per cent. *Nature* **601**, 573–578 (2022).

3. Lin, X. *et al.* In situ growth of graphene on both sides of a Cu–Ni alloy electrode for perovskite solar cells with improved stability. *Nat Energy* **7**, 520–527 (2022).

4. Zhang, S. *et al.* Printable and Homogeneous NiO x Hole Transport Layers Prepared by a Polymer-Network Gel Method for Large-Area and Flexible Perovskite Solar Cells. *Adv Funct Mater* **31**, 2106495 (2021).

5. Peng, W. *et al.* Reducing nonradiative recombination in perovskite solar cells with a porous insulator contact. *Science* **379**, 683–690 (2023).

6. Bai, Y. *et al.* Initializing film homogeneity to retard phase segregation for stable perovskite solar cells. *Science* **378**, 747–754 (2022).

7. Tan, L. *et al.* Combined Vacuum Evaporation and Solution Process for High-Efficiency Large-Area Perovskite Solar Cells with Exceptional Reproducibility. *Advanced Materials* **35**, (2023).

8. Turren-Cruz, S.-H., Hagfeldt, A. & Saliba, M. Methylammonium-free, high-performance, and stable perovskite solar cells on a planar architecture. *Science* **362**, 449–453 (2018).

9. Li, Z. *et al.* 24.64%-Efficiency MA-Free Perovskite Solar Cell with Voc of 1.19 V Enabled by a Hinge-Type Fluorine-Rich Complex. *Adv Funct Mater* **33**, (2023).

10. Gharibzadeh, S. *et al.* Two birds with one stone: dual grain-boundary and interface passivation enables >22% efficient inverted methylammonium-free perovskite solar cells. *Energy Environ Sci* **14**, 5875–5893 (2021).

11. Pan, T. *et al.* Surface-Energy-Regulated Growth of α-Phase Cs0.03FA0.97PbI3 for Highly Efficient and Stable Inverted Perovskite Solar Cells. *Advanced Materials* 2208522 (2023).

12. Momma, K. & Izumi, F. VESTA 3 for three-dimensional visualization of crystal, volumetric and morphology data. *J Appl Crystallogr* **44**, 1272–1276 (2011).